Published May 31, 2019

Special Section: Nonuniform Flow across Vadose Zone Scales

Core Ideas

- For preferential flow modeling, different macropore types must be considered.
- A method was developed for separating biopores and cracks in 3D images from XRCT.
- The method enabled a more objective determination of structuring element sizes.
- The voxel-based approach was found useful for quantification of macropore types.

Separation of Soil Macropore Types in Three-Dimensional X-Ray Computed Tomography Images Based on Pore Geometry Characteristics

Martin Leue,* Daniel Uteau-Puschmann, Stephan Peth, Jens Nellesen, Radka Kodešová, and Horst H. Gerke

In structured soils, earthworm burrows, root channels, shrinkage cracks, and interaggregate spaces form complex macropore networks. Depending on the type and morphological properties, each macropore surface type is coated with specific organo-mineral compounds, differently affecting sorption and mass exchange during preferential flow and turnover processes. For a quantitative, macropore type–specific analysis using X-ray computed tomography (XRCT) with subsequent three-dimensional (3D) image analysis, a discrimination of biopores from cracks and interaggregate spaces is necessary. We developed a method that allows separating biopores from other larger macropores in 3D images from XRCT of intact soil cores. An image-processing workflow using the MAVI (Modular Algorithms for Volume Images) software framework ToolIP (Tool for Image Processing) was created to handle XRCT 3D images. Masking steps enabled to retain the surface roughness in the resulting two images of separated biopores and cracks. As a key point, the sizes of the structuring elements used in the spherical opening and dilation were objectively determined. For this purpose, maximum differences in the pore shapes between the 3D images of cylindrical biopores vs. more flat cracks and unregularly interaggregate spaces were focused. At the given resolution of 231-μm voxel edge length, an optimum size of 2.5 voxels was found for both processing steps. The voxel-based approach is applicable to XRCT 3D images of different spatial resolution and appears useful for the quantification of physicochemical surface properties of different macropore types for soil volumes, enabling a more precise description of preferential flow and transport.

Abbreviations: 3D, three-dimensional; EHR, equivalent hydraulic radius; OM, organic matter; vx, voxel; XRCT, X-ray computed tomography.

M. Leue and H.H. Gerke, Research Area 1 Landscape Functioning, Working Group Hydropedology, Leibniz Centre for Agricultural Landscape Research (ZALF), Eberswalder Str. 84, D-15374 Müncheberg, Germany; D. Uteau-Puschmann and S. Peth, Faculty of Ecological Agriculture, Dep. of Soil Science, Univ. Kassel, Nordbahnhofstr. 1a, D-37213 Witzenhausen, Germany; J. Nellesen, RIF–Institut für Forschung und Transfer, Joseph-von-Fraunhofer-Str. 20, D-44227 Dortmund, Germany; R. Kodešová, Faculty of Agrobiology, Food and Natural Resources, Dep. of Soil Science and Soil Protection, Czech Univ. of Life Sciences Prague, Kamýcká 129, CZ-16521 Prague 6, Czech Republic. *Corresponding author (Martin.Leue@zalf.de).

Received 14 Sept. 2018.
Accepted 20 Feb. 2019.

Citation: Leue, M., D. Uteau-Puschmann, S. Peth, J. Nellesen, R. Kodešová, and H.H. Gerke. 2019. Separation of soil macropore types in three-dimensional x-ray computed tomography images based on pore geometry characteristics. Vadose Zone J. 18:180170. doi:10.2136/vzj2018.09.0170

In structured soils, earthworm burrows, root channels, shrinkage cracks, and interaggregate spaces form a complex macropore network that is relatively persistent in the subsoil even under arable land use (e.g., Pagenkemper et al., 2013; Zhang et al., 2018). Macropores are biogeochemical hotspots (Bundt et al., 2001; Kuzyakov and Blagodatskaya, 2015), where turnover processes are accelerated by increased aeration and nutrient supply. They can also serve as preferential flow paths during rainstorm events (e.g., Jarvis, 2007).

The properties of macropores depend on morphological (i.e., geometrical) properties of the pore spaces as well as on physicochemical properties of the pore surfaces. During preferential flow, these structural surfaces provide an effective interface area for mass exchange between the preferential flow pore domain and the soil matrix (Gerke, 2012) and for sorption and exchange processes of preferentially transported chemicals (Fér et al., 2018; Lin, 2010).

In the clay-illuvial horizons of Luvisols (Bt horizons), the surfaces of aggregates and cracks are characteristically coated by clay organic material. These coatings contain increased organic carbon contents (Leue et al., 2018), a fact that was also reported for the surfaces of earthworm burrows and the drilosphere around these biopores (Don et al.,

2008; Pagenkemper et al., 2015). However, as a crucial point, crack coatings in Bt horizons revealed a significantly different organic matter (OM) composition as compared with other macropore surfaces (Leue et al., 2016, 2017). The OM along cracks, bound and stabilized by accumulated clay minerals, was found to be rich in relatively stable, high molecular compounds. As well, the coatings along cracks result in less surface roughness compared with earthworm burrows (Leue and Gerke, 2016). This implies differences in the OM accumulation and turnover at different macropore types and in physicochemical surface properties such as wettability (Leue et al., 2015), which is relevant for preferential transport in soils. Macroscale and microscale images of dye tracer distribution in Bt horizons showed that tracer is predominantly and quickly distributed by large biopores but is subsequently distributed by smaller macropores and matrix pores (Kodešová et al., 2012). Hence, it appears necessary to combine these different macropore surface properties with quantitative information on macropore densities and geometries. Thus, a separate consideration of the two main macropore types (i.e., biopores and cracks) is needed for improved quantification of macropore effects on preferential flow and turnover processes.

X-ray computed tomography (XRCT) with subsequent three-dimensional (3D) analysis of tomographic images has frequently been used to investigate intact soil structures and macropore networks noninvasively (Perret et al., 1999, 2002). Briefly, the attenuation of a bundle of X-rays by different phases of a soil sample, which is exposed in different angles to the X-rays, yields a set of radioscopic images of the soil sample. From these projections, a 3D tomographic image of the soil specimen can be reconstructed that consists of a 3D array of (homogeneous) cubic volume elements (so-called voxels, vx). Each voxel holds a reconstruction value that approximates the attenuation properties (i.e., the attenuation coefficient for an effective X-ray energy) in that voxel region. From this 3D voxel matrix, macropores can be identified and quantified by using 2D and/or 3D image analysis techniques. Under restriction of a relatively coarse spatial resolution, XRCT analyses can be performed for relatively large soil volumes: Pagenkemper et al. (2013, 2015) investigated biopores in soil monoliths of 700 mm in height and 200 mm in diameter. Sammartino et al. (2015) combined XRCT analyses of macropore networks in soil cores of 150 mm in height and 135 mm in diameter with quasi-simultaneous infiltration experiments to identify and quantify preferential flow paths.

One fundamental methodological challenge of image processing is the development of more objective procedures for the determination of parameter thresholds needed in several operational steps to conserve reproducibility of data analyses. Several statistical methods used for image segmentation in 3D image data are well described (e.g., Iassonov et al., 2009; Wang et al., 2011). However, for the separation of different macropores in segmented datasets, methods that aim at identifying and separating biopores (i.e., large earthworm burrows or root channels) from nonbiopores are limited. One approach (e.g., Capowiez et al., 2011; Pagenkemper et al., 2013, 2015) uses a threshold obtained from the image-derived pore size distribution to separate biopores from other pores. However, assuming that biopores include a wide range of sizes due to the variety of soil invertebrates, the application of a solely volume-sized threshold appears critical. Furthermore, the approach does not allow quantifying the sensitivity of pore morphology parameters with respect to different data processing steps.

Zhang et al. (2015, 2018) separated biopores and nonbiopores in 3D images obtained by XRCT measurements from small soil cores (50 mm in height, 47 mm in diameter). The approach consisted of a stepwise subtraction of objects (i.e., pores) with defined volumes and shapes (i.e., ratio between pore length and pore equivalent radius) from the entire dataset. As a consequence, disconnected single pores of different sizes (including the "noise") were removed as well as these pores, which were dissimilar in shape compared with biopores. Such use of pore shape parameters seems promising. However, the definition of thresholds has not been examined, in particular with respect to basic processing operations frequently applied to 3D images, such as spherical opening and dilation.

The objective of this work was to develop a method to separate biopores from other larger macropores, which both could act as preferential flow paths, in 3D images from XRCT measurements of soil cores. This method should be applicable for quantification of the physicochemical surface properties of different macropore types in preferential flow models for structured soils. The main focus was to independently determine the size of structuring elements used in the processing steps of spherical opening and dilation. The selection of such separation criteria was primarily based on the analysis of pore shape parameters.

Materials and Methods

Soils and Sampling

For this methodological study, two soil cores (250-mm height, 200-mm diameter) were used, obtained from the Bt horizon of a Haplic Luvisol developed from loess and from glacial till. The loess-derived Luvisol was from the experimental site of Hnevceves in the northern Czech Republic (near Hradec Kralove), and the till-derived Luvisol was from the experimental site CarboZALF-D of Holzendorf in northeastern Germany (near Prenzlau). Both subsoil Bt horizons were selected because of the similar pedologic development and structuring with cracks, fissures, and earthworm burrows as potential preferential flow paths on a coarser and a finer textured parent material (Table 1). More information on soils and sites can be found for the loess-derived Luvisol in Kodešová et al. (2011) and Fér and Kodešová (2012) and for the till-derived Luvisol in Rieckh et al. (2012, 2014).

At the sampling sites, the topsoil (here Ap and Al horizons) was removed. A parallel soil pit was excavated to facilitate the sampling and to identify the soil horizons. Soil sampling in the Bt horizons was performed as described in Rogasik et al. (1997) with acrylic glass cylinders (250 mm height, 200 mm inner diameter), from which a representative central part of 50-mm height was used in the analysis.

Table 1. General information on the two sampled Haplic Luvisols sites and soil properties of the sampled Bt horizons (Leue et al., 2018).

Site name	Longitude	Latitude	MAP†	MAT‡	Parent material	Land use	Depth of Bt	pH ($CaCl_2$)	Clay	Silt	Sand	Soil organic C
			mm yr^{-1}	°C			cm		%			g kg^{-1}
Hnevceves	15°43′3″	50°18′47″	618	8.5	loess	arable	34–57	6.3	29.4	61.4	9.2	4.8
Holzendorf	13°47′11″	53°22′45″	501	8.7	glacial till	arable	31–70	6.4	20.3	25.6	54.1	3.9

† Mean annual precipitation.
‡ Mean annual temperature.

X-Ray Computed Tomography Measurements

The soil cores were tomographically imaged in field-moist condition at the RIF Institute for Research and Transfer, Dortmund, Germany, with a vtomex L 240 μCT scanner (phoenix X-ray, GE Sensing and Inspection Technologies), which is equipped with a flat panel detector (XRD 1620, PerkinElmer). The detector has a sensitive area of 410 by 410 mm and consists of a 2048- by 2048-pixel resolution with a pitch of 200 μm. Each soil core was scanned in two height steps, which results in two overlapping 3D XRCT images to achieve high spatial resolution. The scan parameters were: maximum X-ray photon energy = 160 keV, current = 1000 μA, 1200 cone-beam projections, circular scan trajectory, and a 1-mm Cu pre-filter to minimize the beam hardening. For tomographic reconstruction, the software datos|x, version 1.5.0.15 (phoenix X-Ray, GE Sensing and Technologies) was used, which is based on a modified Feldkamp algorithm (Feldkamp et al., 1984). The achieved voxel resolution was 231 μm in all spatial directions.

Image Analyses

For each soil core, the overlapping slices of the two scanning height steps were merged and renumbered; images without soil information were deleted. All image pre- and post-processing was done with the software MAVI (Modular Algorithms for Volume Images; Fraunhofer Institute for Industrial Mathematics, 2012). The algorithms were implemented in the MAVI framework ToolIP (Tool for Image Processing), where numerous 3D analytical solutions can be automatized by means of flow processing charts. About 7 mm of the outermost layer of the soil cores was masked out by a binary cylinder mask to remove the cylinder wall as well as any disturbed soil pore space close to the wall.

Cone defects due to beam hardening effects during the XRCT measurements were corrected by applying a mean correction filter in radial direction. This application was performed slice by slice to compensate for the radial gray gradient. A global threshold was calculated for each slice using Otsu's method (Otsu, 1979). For the presented method development, a test dataset of 201 slices (i.e., 46.43-mm height) from each soil core (loess and glacial till) was used.

Workflow: Separation of Macropore Types

The entire workflow of the ToolIP software is illustrated in Fig. 1. In the following, parameter values are expressed as voxels (vx) because it is easier to adjust and to follow the operational steps by using integers compared with millimeter-based floats. More importantly, the voxel-based method can be more easily applied to other XRCT image data with different spatial resolutions (i.e., voxel edge lengths).

The previously segmented slices were loaded as a complete 3D image (Fig. 1, Step 1; Fig. 2a). After inversion of the foreground and background, a Fill-Hole algorithm (Fig. 1, Step 2) was used to remove small isolated matrix objects of radii ≤2 vx, which would

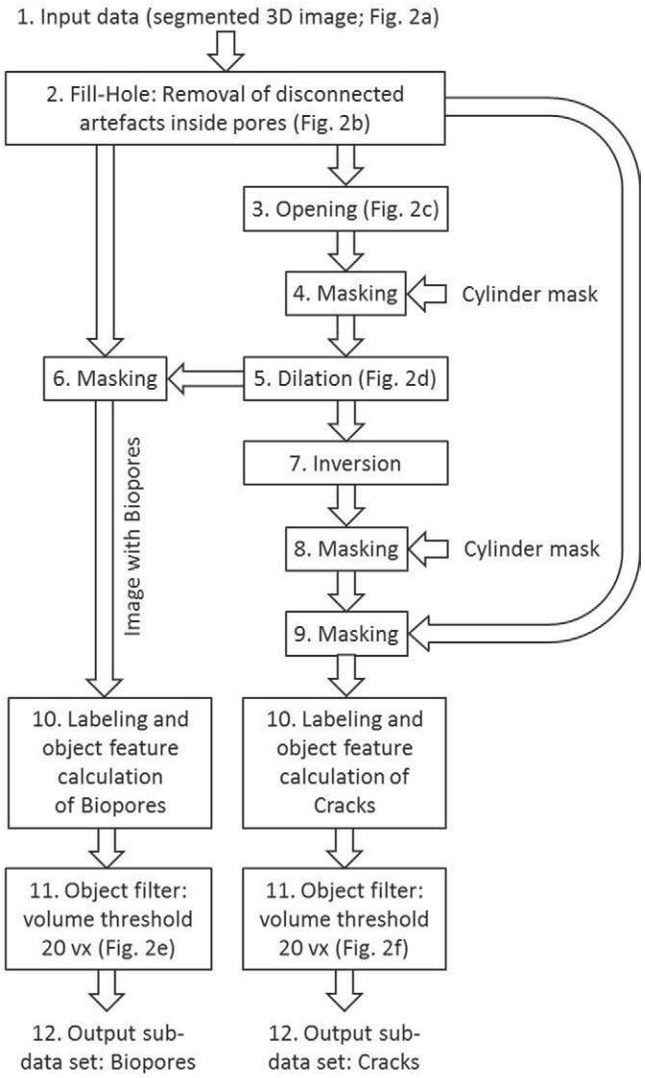

Fig. 1. Workflow of three-dimensional (3D) image analysis using the MAVI software framework ToolIP (Fraunhofer Institute for Industrial Mathematics, 2012).

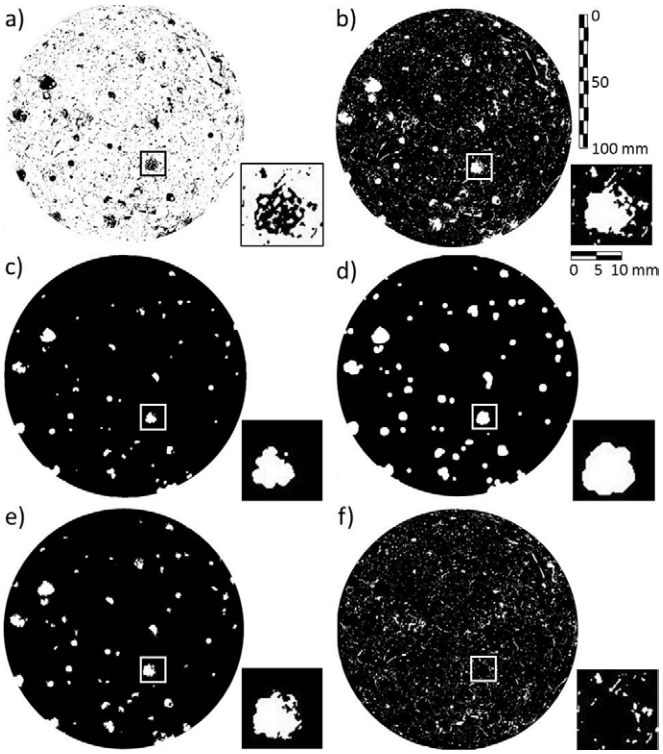

Fig. 2. Horizontal slices of a soil core of 186 mm in diameter obtained from the Bt horizon of a loess-derived Luvisol. Stepwise results of the image analysis: (a) segmented image, (b) fill-hole, (c) spherical opening, (d) spherical dilation, (e) image of remaining biopores, and (f) image of remaining cracks and interaggregate spaces. Detail pictures enlarge a biopore (earthworm burrow) inside a framed area of 16-mm edge length.

represent physically impossible structures, such as soil particles floating in the large pore spaces (Fig. 2b). Then, the images were split into two different images, of which one was used to provide the more cylindrical large biopores of different sizes (denoted as biopores; Fig. 1, left-hand side), and the other one was used to extract cracks and interaggregate spaces (denoted as cracks; Fig. 1, right).

Isolation of Large Pores by Spherical Opening

For the crack data, a spherical opening was applied (Fig. 1, Step 3). A standard opening algorithm consists of an erosion step (Fig. 3, Detail 2) and a dilation step (Fig. 3, Detail 3), which in sum subtract a layer of voxels from the boundaries of the pores (Fig. 2c). The size (i.e., the radius) of the structuring element used in the opening (E_O) determines the thickness of the subtracted layer. In doing so, all pores smaller than the doubled radius (i.e., the diameter) of E_O are removed (Fig. 2c and Fig. 3, Detail 3). Thus, the radius of E_O coincidentally determines the size and number of the remaining pores (i.e., objects in the dataset). For the dataset processed by the Fill-Hole algorithm, a spherical opening filter with E_O = 2.5 vx radius (equal to 0.578 mm) was applied to the pores (Fig. 1, right side). The size of E_O was determined individually for the two soil samples by the procedure described below.

As result of the opening, only pores with large equivalent diameters of >1.156 mm remained and were used to mask out and

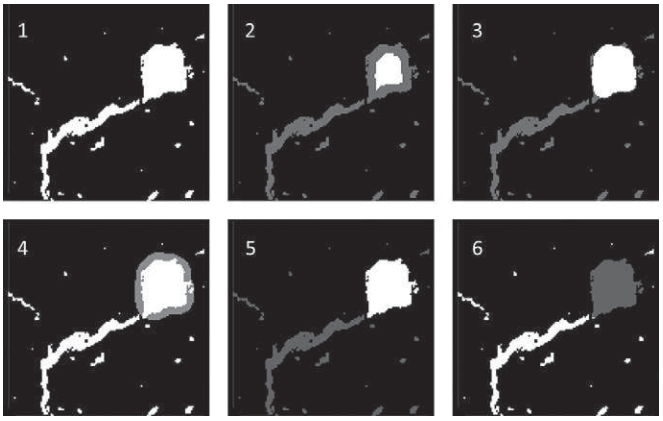

Fig. 3. Principle of separation of macropore types in detail (1 pixel = 231 by 231 μm). Original two-dimensional image (1) of a biopore (upper right corner) and cracks (from center to lower left corner) and interaggregate spaces. Opening procedure including the inherent steps of erosion (2) and dilation (3); the size of the structuring element in the opening determines the thickness of the applied layer (gray area). Independent dilation (4) as processing step for the subsequent masking. The size of the structuring element in this step determines the thickness of the applied layer (gray area). Resulting biopore (5) and cracks (6) remaining after masking.

analyze these large biopores after the following dilation. Because the images were square and the sample appeared cylindrical, the corners of each image in the stack were masked out by a circular mask (Fig. 1, Steps 4 and 8). The radius of the cylinder mask was 7 mm smaller than the radius of the soil core to exclude the outermost rim of the soil core that had been compacted or smeared during the sampling.

Preserving the Pore Roughness by Spherical Dilation

The opening created smoother surfaces that would alter the morphological parameters (in particular the pore surface). Thus, a spherical dilation was applied to the crack image (Fig. 1, Step 5) to preserve the pore roughness as determined by the spatial resolution of the XRCT scans. The dilation adds a layer of voxels to the boundaries of the pores (Fig. 2d and 3, Detail 4) remaining from the spherical opening. The size (i.e., the radius) of the structuring element (E_D) used in the dilation determines the thickness of the added layer and thus affects the number and size of the remaining pores. Note that E_D needs to be equal or greater than E_O. For the dataset processed by the opening algorithm, a spherical dilation (Fig. 1, Step 5) with a structuring element (E_D) of 2.5 vx radius (0.578 mm) was applied to the remaining pores.

Macropore Separation by Masking

The 3D image resulting from the dilation was used as a mask on the original image from the Fill-Hole step to obtain all large biopores with their original surface roughness (Fig. 1, Step 6). Next, the 3D image was inverted (Fig. 1, Step 7) and masked out by a circular mask (Fig. 1, Step 8) to remove the corners of the image. The result was used as a mask for the original images (Fig. 1, Step 9) to remove the large and cylindrical-like biopores (Fig. 2e

and Fig. 3, Detail 5) and let the smaller and thinner pores of cracks and interaggregate spaces remain (Fig. 1, right; Fig. 2f; and Fig. 3, Detail 6). The sum of the biopore image and the crack image is equal to the original image.

Calculation of Morphological Pore Properties (Object Features)

Among the pores (i.e., the objects), we aimed to separate the more elongated and large biopores (earthworm burrows) from smaller pores of more heterogeneous shape (cracks, interaggregate spaces, and small biopores). For testing different morphological properties that are best suited to characterize and separate the pore types, the objects of biopores and cracks were labeled, and the following object features were calculated for each object (Fig. 1, Step 10): geometrical center position (x, y, z), volume (V), surface area (S), size (x, y, z dimensions), diameters (mean and SD), integral of mean curvature (M), and the three isoperimetric shape factors (f_1,f_2,f_3).

The integral of mean curvature M measures the mean curvature of the interface between pore(s) and solid, considering convex and concave radii:

$$M(X)=\frac{1}{2}\int_{\delta X}\left[\frac{1}{r_1}+\frac{1}{r_2}\right]\mathrm{d}s \quad [1]$$

where r_1 and r_2 are the minimum and the maximum radii of the curvature for the surface element ds of an object X (Vogel et al., 2010). In case of elongated objects, M can be used to measure the length of an object (Fraunhofer Institute for Industrial Mathematics, 2012). The shape factors were defined as (Vecchio et al., 2012; Fraunhofer Institute for Industrial Mathematics, 2012)

$$f_1=6\sqrt{\pi}\frac{V}{\sqrt{S^3}} \quad [2]$$

$$f_2=48\pi^2\frac{V}{M^3} \quad [3]$$

$$f_3=4\pi\frac{S}{M^2} \quad [4]$$

These factors describe the shape of an object (here a pore) using the basic morphologic parameters V, S, and M. In the case of a ball, the value of each shape factor equals 1. Among the shape factors, f_2 decreased with increasing elongation of the objects and was found to be most sensitive with respect to differences between biopores and cracks. Higher f_2 values of an object imply higher isotropy in all directions (Fraunhofer Institute for Industrial Mathematics, 2012). Visual inspection revealed that long elongated (anisotropic) biopores exist in the soil samples; therefore, it appeared reasonable to search for a maximum difference in the mean f_2 values between biopores and cracks.

Noise Reduction by Filtering

A subsequent 3D object filter allowed to filter objects by specific properties. A volume threshold of minimum 20 vx (0.25 mm^3) was applied (Fig. 1, Step 11) to remove small isolated objects that may have occurred by the combined effect of noise and segmentation. This filtering step ensured that only those objects were analyzed that were confirmed to be pores. Further, only those pores that may be relevant for preferential flow processes should be considered (Perret et al., 1999). The output spreadsheets, including the morphological data, were saved as comma-separated values files for later analyses (Fig. 1, Step 12).

Optimized Sizes of Structuring Elements E_O and E_D

Theoretically, the sizes of E_O and E_D can be defined randomly. In most cases, they will be determined after visual inspection of the output images. However, here we propose a method to determine the optimum sizes of E_O and E_D by analyzing their quantitative effects on the output data. We expect the existence of optimum sizes for E_O and E_D because both parameters are important parts of the proposed method and are supposed to be suited for separating biopores from cracks as clearly as possible. In a first step, the workflow was performed several times using E_O with radii of 1.5, 2.0, 2.5, 3.0, 3.5, 4.0, and 5.0 vx edge lengths (0.35, 0.46, 0.58, 0.69, 0.81, 0.92, and 1.16 mm). During each run, the size of the structuring element used in the spherical dilation (E_D) was equal to E_O. For each size of E_O (i.e., for each run), the values of the object features were calculated for biopores cracks from the two sites (loess and till).

For finding optimal sizes of E_O, the pore shape and total pore surface area were considered. The output spreadsheets were used in MS Excel to analyze the object features and to calculate relevant parameters as well as their summed and median values and SDs. As one important additional parameter describing the shape of pores, the surface-to-volume ratio was calculated for each object in the morphological datasets (S/V ratio).

The differences in the pore shapes should be maximized between the images because biopores have different shapes compared with cracks and interaggregate spaces. Thus, the median values of the shape factors f_1,f_2, and f_3 (see object features above) and of the S/V ratio were calculated for every size of E_O. The differences (δ) in median f_1,f_2,f_3, and S/V between biopores and cracks were calculated and normalized [0;1]. The normalized differences ($\delta f_{1,2,3}$ and $\delta S/V$) were plotted against E_O, and the intersection of the regression lines was assumed to yield the optimum size of E_O.

Furthermore, it appeared reasonable to maximize the total surface area (S_{tot}) of all pores (i.e., as the sum of biopores and cracks). This means that the opening should avoid "losing" surfaces by removing too many pores in case of increasing E_O. The S_{tot} was calculated as the sum of S of all biopores and cracks. Differences in S_{tot} between different sizes of E_O were calculated as the percentage of loss or gain in relation to S_{tot} of the starting size of E_O = 1.5 vx.

The optimal size of E_D was determined analogous to E_O by running the workflow with stepwise increasing sizes of E_D in every run using element radii of 2.5, 3.0, 3.5, 4.0, 5.0, 6.0, and 7.0 vx edge lengths (equal to 0.58, 0.69, 0.81, 0.92, 1.16, 1.37, and 1.62 mm); E_O was kept constant (2.5 vx).

Complemental Morphological Parameters

The effect of changing sizes of E_O and E_D was also tested for complemental morphological parameters that have been frequently used for pore space quantification and, in particular, for pore type separation. Moreover, they are highly relevant for describing potential preferential flow paths. As the most important soil structural parameter, the total pore volume (V_{tot}) of the soil cores was calculated as the ratio between the summed volume of all objects (i.e., pores) in a soil core and the total volume of the soil core. Due to the relatively coarse spatial resolution of 231 μm vx edge length, this value of V_{tot} presents only the volume of the larger pores and macropores that are most relevant for preferential flow. The tortuosity (τ) and the equivalent hydraulic radius (EHR) were calculated because both have been used for macropore separation by Zhang et al. (2015) in a method based on histogram thresholds. According to Luo et al. (2010), for each *i*th identified pore object, the value of τ was calculated as the ratio between total actual macropore length, here represented by the integral of mean curvature (M), to the total length, represented by the maximum size of an object in the x, y, or z direction:

$$\tau_i = \frac{M_i}{\max(x,y,z)_i} \quad [5]$$

The EHR of each *i*th identified pore object was calculated as ratio between V and total length of the macropore (Luo et al., 2010), the latter represented by the maximum size of an object in x, y, or z direction:

$$\mathrm{EHR}_i = \frac{V_i}{\max(x,y,z)_i} \quad [6]$$

The median values of τ and EHR were calculated for biopores as well as for cracks obtained from different sizes of E_O and E_D (i.e., each run) and for soils of both sites.

Validation of Macropore Types

A straightforward algorithm was developed using MS Excel to identify objects in the morphological datasets as biopores or cracks to check the morphological properties of individual pores and thus to prove the methodology of the image processing. Biopores that potentially act as preferential flow paths were defined as objects elongated predominantly in the z direction (the z axis coincides to the direction of gravitational force). Thus, the first condition was that the z size was greater than the mean value plus SD in all the three main dimensions (x, y, z). For large biopores, the second condition was a length threshold for the z size of a maximum 201-vx edge length (46.4 mm) corresponding to the z extension of the image. Objects were denoted as cracks if one dimension was smaller than the mean value plus standard deviation of all three main dimensions (x, y, z). Objects were denoted as large cracks if one of these dimensions reached an elongation of 201 vx, corresponding to the height of the test data set.

Results

Spherical Opening: Size of Structuring Element E_O

For the datasets from both Luvisol sites, $\delta S/V$ increased while δf_2 decreased with increasing sizes of E_O (Fig. 4). Shape factor f_1 showed no continuous trend for increasing sizes of E_O, and f_3 showed a very similar trend compared with f_2; thus, results are presented only for f_2. The intersection between the fitted regression lines of $\delta S/V$ and δf_2 indicated an optimum E_O size of ~2.5 vx. For this E_O size, the greatest differences between biopores and cracks could be obtained when the two shape parameters S/V and f_2 were considered. In terms of the absolute values (Table 2), S/V levels varied for biopores between 1.258 and 0.516 and for cracks between 1.873 and 1.907. A fitting of linear instead of exponential functions revealed slightly larger optimum E_O sizes of ~2.8 vx but yielded smaller values of R^2 of ~0.83 (not shown).

For both sites, the S_{tot} summarized for biopore as well as for cracks decreased with increasing E_O sizes (Table 2). The relative decrease in S_{tot} between the starting (1.5 vx) and the end size of E_O (5.0 vx) was 60% (loess) and 9% (till). At E_O = 2.5 vx, the S_{tot} values of the loess pores were approximately three times higher compared with the S_{tot} of the till pores.

For the two sites, the numbers of biopores as well as of cracks and aggregate spaces decreased with increasing E_O sizes (Table 2). The total volume of large macropores (V_{tot} of biopores and cracks) decreased with increasing E_O sizes for the loess sample; however, it remained nearly constant for the till sample (Table 3). Applying the object volume threshold of $V \geq 20$ vx ($V \geq 0.247$ mm^3) and for optimized E_O = 2.5, V_{tot} of the large macropores was 5.78% for the loess and 2.96% for the till sample. The proportions of biopores in V_{tot} were twice (loess) and four times (till) higher than those of the cracks and interaggregate spaces. With increasing E_O,

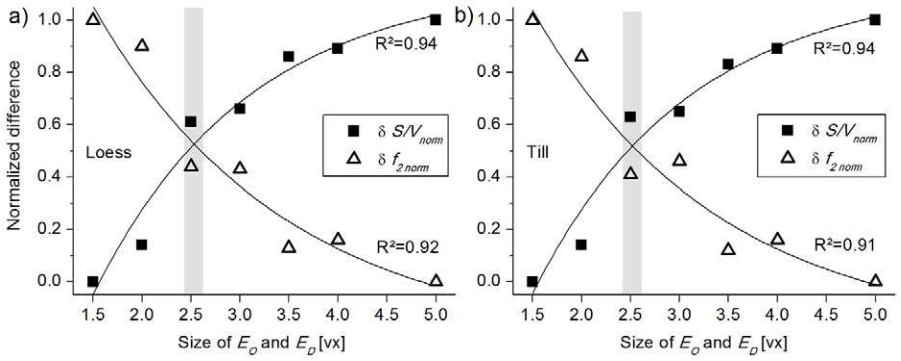

Fig. 4. Differences in the normalized median values of surface/volume ratio ($\delta S/V$) and shape factor 2 (δf_2) between biopores and cracks related to the radius of the structuring element used in the spherical opening (E_O) and dilation (E_D). Curves show fitted exponential regressions; gray areas determined by the intersection of the regression lines indicate the voxel (vx) sizes for optimum E_O sizes. Data from soil cores obtained from (a) loess Bt and (b) till Bt horizons.

Table 2. Total (tot) values of surface area (S), median values (med) of surface/volume ratio (S/V) and shape factor f_2, and number calculated for biopores (Biop) and cracks (Cr) obtained from different sizes of E_O ($E_D = E_O$).

Size E_O and E_D	S_{tot}			S/V_{med}, Biop	f_{2med}, Biop	No. Biop	S_{tot}, Cr	S/V_{med}, Cr	f_{2med}, Cr	Cr, n
	Biop + Cr	Biop + Cr	(Biop)							
vx†	px‡	cm^2	px				px			
					Loess					
1.5	6,796,754	3627	3,097,713	1.258 (0.234)§	0.573 (0.003)	6063	3,699,042	1.898 (0.230)	0.115 (0.001)	21,915
2.0	6,761,621	3608	2,580,197	1.130 (0.245)	0.536 (0.004)	4213	4,181,423	1.873 (0.257)	0.118 (0.002)	19,715
2.5	4,508,242	2406	1,652,691	0.792 (0.194)	0.361 (0.006)	1161	2,855,552	1.888 (0.294)	0.131 (0.002)	14,531
3.0	4,202,774	2243	1,508,398	0.761 (0.236)	0.359 (0.007)	989	2,694,376	1.894 (0.296)	0.134 (0.002)	14,045
3.5	3,389,746	1809	1,174,100	0.614 (0.200)	0.240 (0.010)	453	2,215,646	1.902 (0.296)	0.138 (0.002)	13,029
4.0	3,149,240	1680	1,048,289	0.593 (0.220)	0.253 (0.014)	363	2,100,951	1.903 (0.297)	0.140 (0.002)	12,757
5.0	2,689,455	1435	798,140	0.516 (0.396)	0.19 (0.018)	188	1,891,314	1.907 (0.296)	0.142 (0.002)	12,309
					Till					
1.5	1,644,003	877	975,761	1.236 (0.277)	0.559 (0.009)	976	668,242	1.863 (0.234)	0.135 (0.003)	3826
2.0	1,616,852	863	879,951	1.104 (0.281)	0.515 (0.010)	702	736,901	1.832 (0.263)	0.137 (0.003)	3702
2.5	1,522,362	812	683,180	0.724 (0.238)	0.365 (0.015)	235	839,182	1.804 (0.317)	0.136 (0.004)	3108
3.0	1,522,811	813	658,792	0.706 (0.291)	0.380 (0.016)	222	864,019	1.806 (0.325)	0.135 (0.004)	3055
3.5	1,521,716	812	601,644	0.578 (0.358)	0.270 (0.017)	147	920,071	1.806 (0.336)	0.138 (0.004)	2914
4.0	1,503,017	802	572,072	0.536 (0.344)	0.281 (0.019)	133	930,945	1.808 (0.348)	0.137 (0.004)	2858
5.0	1,487,912	794	511,484	0.460 (0.326)	0.232 (0.022)	76	976,428	1.811 (0.356)	0.139 (0.004)	2769

† Voxels.
‡ Pixels.
§ Values in parentheses are SD.

Table 3. Total (tot) and relative pore volumes (V), median values (med) of tortuosity (τ) and equivalent hydraulic radius (EHR), calculated for biopores and cracks obtained from different sizes of E_O ($E_D = E_O$).

Size E_O and E_D†	V_{tot}			τ_{med}		EHR_{med}		Large biopores‡	Large cracks‡
	Biopores + cracks	Biopores	Cracks	Biopores	Cracks	Biopores	Cracks		
vx	vx								
					Loess				
1.5	7,362,217 (7.47)§	5,282,368 (5.36)	2,079,849 (2.11)	5.86	5.54	11.63	4.67	17	0
2.0	7,308,381 (7.42)	4,825,439 (4.90)	2,482,942 (2.52)	6.34	5.55	15.90	4.83	18	3
2.5	5,691,449 (5.78)	3,843,494 (3.90)	1,847,955 (1.88)	6.44	5.43	36.91	4.60	14	0
3.0	5,421,322 (5.50)	3,656,485 (3.71)	1,764,837 (1.79)	6.81	5.41	42.64	4.55	13	0
3.5	4,637,645 (4.71)	31,66,270 (3.21)	1,471,375 (1.49)	6.90	5.37	66.94	4.46	9	0
4.0	4,366,384 (4.43)	2,953,917 (3.00)	1,412,467 (1.43)	7.40	5.36	82.52	4.43	9	0
5.0	3,764,568 (3.82)	2,493,346 (2.53)	1,271,222 (1.29)	7.61	5.35	122.1	4.40	8	1
					Till				
1.5	2,982,071 (3.03)	2,589,506 (2.63)	392,565 (0.40)	5.79	5.42	12.33	4.83	3	0
2.0	2,950,450 (2.99)	2,495,003 (2.53)	455,447 (0.46)	6.23	5.44	16.78	5.00	2	3
2.5	2,913,946 (2.96)	2,308,212 (2.34)	605,734 (0.61)	5.80	5.40	45.27	5.08	4	1
3.0	2,932,252 (2.98)	2,292,328 (2.33)	639,924 (0.65)	6.14	5.41	50.28	5.00	3	1
3.5	2,952,793 (3.00)	2,222,976 (2.26)	729,817 (0.74)	5.88	5.38	71.59	5.00	3	0
4.0	2,961,890 (3.01)	2,188,764 (2.22)	773,126 (0.78)	6.10	5.33	89.48	5.00	2	0
5.0	3,001,773 (3.05)	2,118,234 (2.15)	883,539 (0.90)	6.40	5.32	137.8	5.00	2	0

† vx, voxel; E_O, radius of the structuring element used in the spherical opening; E_D, radius of the structuring element used in the spherical dilation.
‡ Number of large biopores and cracks in the biopore morphological dataset, classified by the validation.
§ Values in parentheses are relative pore volumes as a percentage of the total pore volume.

the proportions of biopores to V_{tot} decreased (loess, from 72 to 66%; till, from 87 to 71%), whereas the proportions of cracks and interaggregate spaces decreased (loess: 28 to 34%; till: from 13 to 29%). The tortuosity (τ) showed no significant trend with increasing E_O, except a slight increase for the biopores of the loess sample (Table 3). In contrast, the EHR strongly increased with E_O for biopores of both sites but remained constant for the cracks. For the loess sample, the number of large biopores in the biopore morphological dataset (as classified by the validation algorithm) generally decreased with increasing E_O (Table 3). The maximum number (n = 18) was found at E_O = 2.0. However, for this E_O size, three pores were still classified as large cracks. In case of E_O = 2.5, no misclassification was found, whereas the number of correctly classified biopores was almost at maximum (n = 14). For the loess sample, the maximum number of biopores was found at E_O = 2.5; however, one pore still was classified as a large crack.

In addition to the general decrease of macropore quantity (i.e., numbers), increasing sizes of E_O and E_D caused a decrease of macropores (i.e., lower frequencies) with small volumes, tortuosity, and equivalent hydraulic radius (Fig. 5). This shifting effect was pronounced for the smaller numbers of biopores but was not as clear for the much higher numbers of cracks. Whereas the loess sample provided a larger number of macropores (i.e., objects), the macropore number of the till sample was smaller. However, the relative decrease in the numbers of pores showed similar levels for both samples.

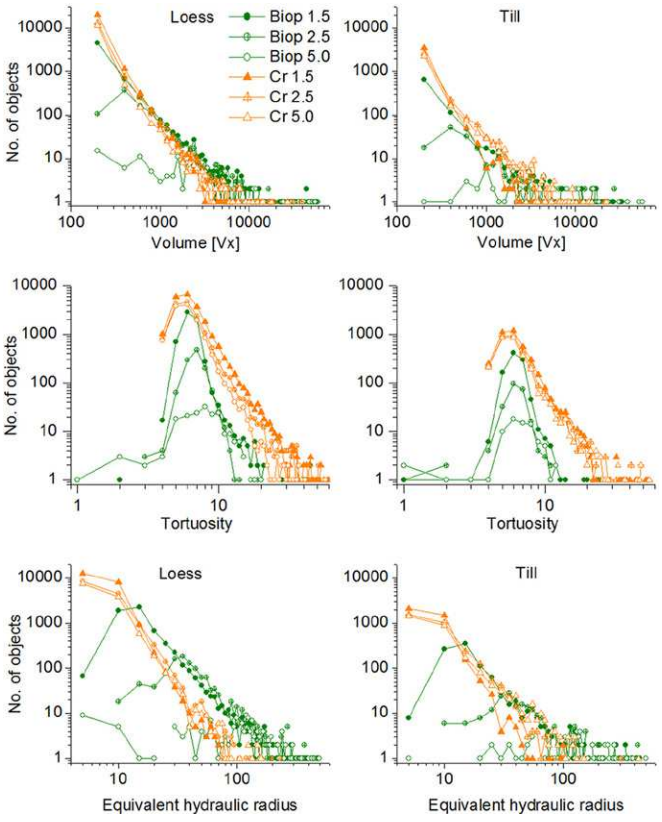

Fig. 5. Histograms of volume, tortuosity, and equivalent hydraulic radius for biopores (green) and cracks (orange) obtained from the three-dimensional images of samples from the loess Bt and the till Bt horizons, for the radius of the structuring element used in the spherical opening (E_O) = the radius of the structuring element used in the spherical dilation (E_D) = 1.5, 2.5, and 5.0.

The effects of increasing E_O and E_D sizes on the numbers and on the assignments of the macropores to either biopores or cracks are exemplarily illustrated by Fig. 6. Higher E_O and E_D sizes result in a separation of smaller numbers of biopores. As a consequence, the rest of the pores are classified as cracks. Again, a size of $E_O = E_D$ = 2.5 vx appears as optimum because all objects appearing as large, cylindrical pores were attributed as biopores. As exemplarily visualized for one single large biopore (Fig. 7), increasing E_O and E_D sizes resulted in a stricter morphological separation between biopores and cracks by a separation of branches and loosely connected parts of the pore cluster. The consequently "smoothing" effect for the biopore was quantified by decreasing values of volume, surface, S/V, τ, and EHR and by increasing values of the shape factors (Table 4). This stricter separation, as visualized (Fig. 6 and 7), was in line with the more pronounced differences in mean f_2 and S/V values (Fig. 4).

Spherical Dilation: Size of Structuring Element E_D

For the constant E_O size of 2.5 vx, $\delta S/V$ and δf_2 decreased with increasing E_D sizes for the datasets from both sites (Fig. 8). The greatest differences between biopores and cracks were found for the smallest E_D sizes (i.e., E_D = 2.5). Regression lines were not

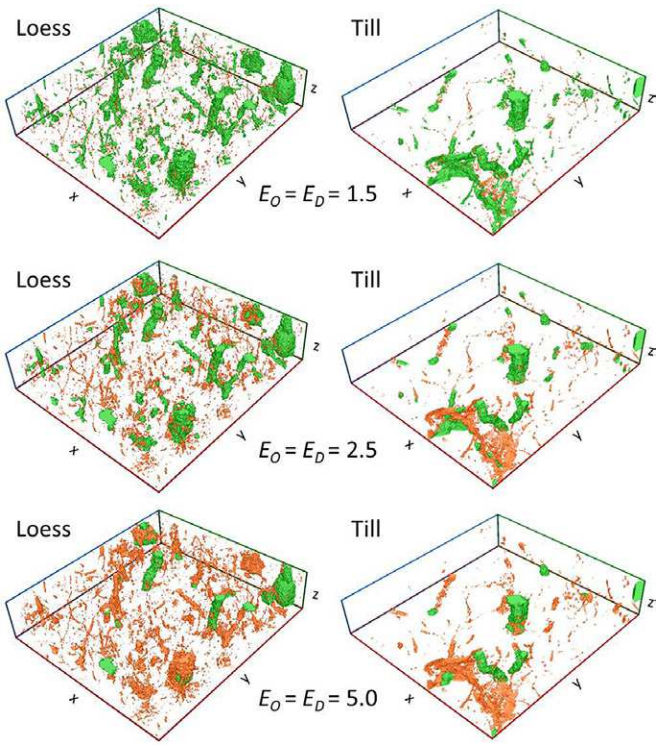

Fig. 6. Three-dimensional plots of the clippings from the data sets of samples from the loess-Bt and the till-Bt. Frame size edge lengths 329 by 362 by 76 voxels (vx) (L by B by H; i.e., 76.0 by 83.6 by 17.6 mm). Biopores are in green; cracks and interaggregate spaces are in red.

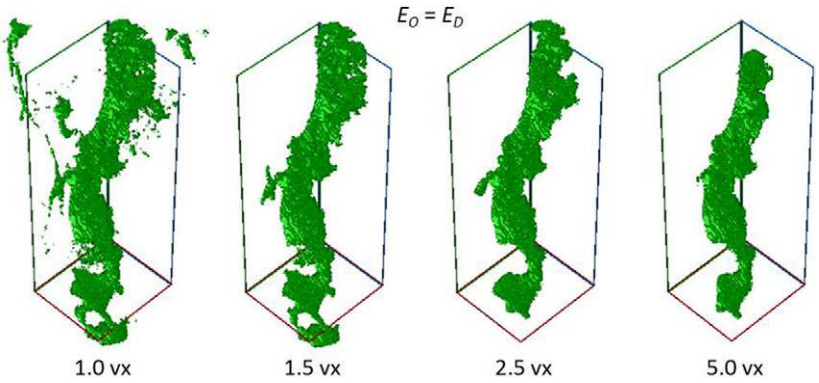

Fig. 7. Effects of increasing sizes of the radii of the structuring elements used in the spherical opening (E_O) and in the spherical dilation (E_D), visualized as an example for one biopore (earthworm burrow segment) from the loess Bt sample. $E_O = E_D$ in all cases. Frame size edge lengths 70 by 70 by 201 voxels (vx) (L by B by H; i.e., 16.2 by 16.2 by 46.4 mm).

Table 4. Volume, surface area, shape factors (f_1, f_2, f_3), surface/volume ratio (S/V), tortuosity (τ), and equivalent hydraulic radius (EHR) calculated for an individual biopore (earthworm burrow segment) from the loess sample after application of different sizes of E_O and E_D. Data corresponding to Fig. 7.

Size E_O†	Size E_D‡	Volume	Surface area	f_1	f_2	f_3	S/V	τ	EHR
voxels			pixels						
1.0	1.0	69,494	42,725	0.084	0.000	0.006	0.615	47.85	345.74
1.5	1.5	56,893	25,224	0.151	0.002	0.063	0.443	11.15	283.05
2.5	2.5	49,103	19,318	0.194	0.005	0.085	0.393	9.07	263.99
5.0	5.0	41,281	15,424	0.229	0.004	0.073	0.374	9.72	245.72

† E_O, radius of the structuring element used in the spherical opening.
‡ E_D, radius of the structuring element used in the spherical dilation.

fitted because both parameters showed the same trend, and thus no intersections could be determined.

For both sites, the S_{tot} summarized for each the biopores and cracks decreased with increasing E_D size (Table 5). The relative increases in S_{tot} between the starting (2.5 vx) and end size of E_D (7.0 vx) were 19% (loess) and 7% (till). The S_{tot} values of the loess pores were approximately three times higher compared with those of the till pores.

With increasing E_D sizes, the number of biopores decreased to E_D = 5 vx and then increased for E_D >5 vx (Table 5) for both sites. The number of cracks and interaggregate spaces of the loess sample increased to E_D = 3.5 vx and then decreased, whereas the number decreased constantly with increasing E_D for the till data. The total pore volume (V_{tot} of biopores and cracks) increased with E_D for both samples (Table 6). With increasing E_D, the proportions of biopores in V_{tot} increased (loess: from 68 to 73%; till: from 79 to 85%), whereas the proportions of cracks and interaggregate spaces decreased (loess: from 32 to 27%; till: from 21 to 15%). The biopores of both sites showed maximum τ and EHR values between E_D sizes of 4.0 and 5.0, with higher levels for the till sample (Table 6). The cracks revealed no significant trends in τ and EHR. For both soils, the number of large biopores (as classified by the validation algorithm) decreased with increasing E_D sizes. However, the number of pores in the biopore morphological dataset classified as large cracks, indicating insufficient separation of the macropore types, increased with E_D.

Under the condition of a constant E_O size (= 2.5 vx), increased E_D sizes yielded lower numbers of biopores with small volumes and tortuosity, effects on equivalent hydraulic radii were without clear trend (Fig. 9). Effects on the frequency distributions were relatively less pronounced for cracks, obviously due to the higher absolute numbers.

The effect of increasing E_D (while E_O = constant = 2.5 vx) is exemplarily visualized for a single biopore in Fig. 10.

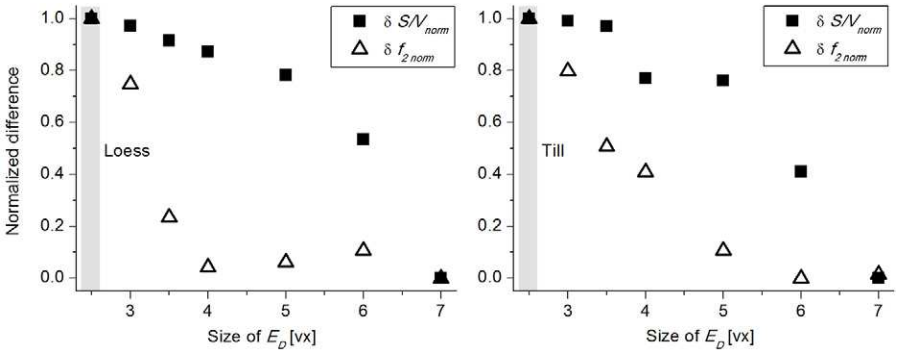

Fig. 8. Differences in the normalized median values of surface/volume ratio ($\delta S/V$) and shape factor 2 (δf_2) between biopores and cracks related to the size (i.e., radius) of the structuring element E_D used in the spherical dilation. For each size of E_D, the radius of the structuring element used in the spherical opening (E_O) was kept constant at 2.5 voxels (vx). Gray areas indicate voxel sizes for optimum E_D sizes. Data from soil cores obtained from (a) loess and (b) glacial till.

Table 5. Total (tot) surface area (S), median values (med) of surface/volume ratio (S/V) and shape factor f_2, and number calculated for biopores (Biop) and cracks (Cr) obtained from different sizes of E_D, while the structuring element used in the opening (E_O) was kept constant (= 2.5 voxels).

	Biopores + cracks		Biopores				Cracks			
Size E_D	S_{tot}	S_{tot}	S_{tot}	S/V_{med}	f_{2med}	n	S_{tot}	S/V_{med}	f_{2med}	n
voxels	pixels	cm^2	pixels				pixels			
					Loess					
2.5	4,508,242	2406	1,652,691	0.792 (0.194)†	0.362 (0.009)	1161	2,855,552	1.888 (0.294)	0.132 (0.003)	14,530
3.0	4,611,543	2461	1,712,232	0.800 (0.203)	0.308 (0.007)	1143	2,899,311	1.887 (0.295)	0.065 (0.002)	14,595
3.5	4,753,606	2537	1,869,649	0.820 (0.195)	0.196 (0.008)	1050	2,883,956	1.886 (0.294)	0.065 (0.002)	14,654
4.0	4,834,032	2579	1,964,338	0.831 (0.224)	0.154 (0.008)	1024	2,869,694	1.884 (0.294)	0.064 (0.002)	14,643
5.0	5,038,954	2689	2,190,160	0.862 (0.366)	0.102 (0.006)	1024	2,848,794	1.884 (0.295)	0.065 (0.002)	14,617
6.0	5,257,069	2805	2,462,776	0.946 (0.516)	0.092 (0.006)	1197	2,794,293	1.884 (0.294)	0.068 (0.002)	14,399
7.0	5,541,297	2957	2,679,235	1.126 (0.555)	0.115 (0.006)	1422	2,862,063	1.883 (0.293)	0.071 (0.002)	14,185
					Till					
2.5	1,522,362	812	683,180	0.724 (0.238)	0.377 (0.592)	235	839,182	1.804 (0.317)	0.136 (0.004)	3107
3.0	1,524,660	814	699,480	0.723 (0.233)	0.329 (1.485)	231	825,180	1.803 (0.316)	0.137 (0.004)	3095
3.5	1,529,625	816	739,671	0.728 (0.241)	0.259 (0.186)	209	789,954	1.806 (0.314)	0.136 (0.004)	3051
4.0	1,534,401	819	763,283	0.740 (0.271)	0.235 (0.139)	207	771,118	1.805 (0.314)	0.135 (0.004)	3022
5.0	1,545,080	824	814,571	0.742 (0.328)	0.164 (0.096)	204	730,510	1.806 (0.313)	0.136 (0.004)	2955
6.0	1,628,890	869	872,477	0.773 (0.500)	0.133 (0.034)	214	756,412	1.815 (0.312)	0.136 (0.004)	2887
7.0	1,641,658	876	914,959	0.800 (0.518)	0.13 (0.021)	224	726,699	1.816 (0.311)	0.137 (0.004)	2822

† Values in parentheses are SD.

Table 6. Total (tot) and relative pore volumes (V), median values (med) of tortuosity (τ) and equivalent hydraulic radius (EHR), calculated for biopores and cracks obtained from different sizes of the structuring element used in the spherical dilation (E_D) while the radius of the structuring element used in the spherical opening (E_O)was kept constant at 2.5 voxels (vx).

Size	V_{tot}			τ_{med}		EHR_{med}		Large	Large
E_D	Biopores + cracks	Biopores	Cracks	Biopores	Cracks	Biopores	Cracks	biopores†	cracks†
vx	vx								
				Loess					
2.5	5,691,449 (5.78)‡	3,843,494 (3.90)	1,847,955 (1.88)	6.44	5.43	36.91	4.60	14	0
3.0	5,788,705 (5.88)	3,909,339 (3.97)	1,879,366 (1.91)	6.81	5.43	38.45	4.60	14	0
3.5	5,935,360 (6.02)	4,071,240 (4.13)	1,864,120 (1.89)	7.05	5.43	38.09	4.60	14	0
4.0	6,022,816 (6.11)	4,170,187 (4.23)	1,852,629 (1.88)	7.67	5.43	39.84	4.60	13	1
5.0	6,234,383 (6.33)	4,401,553 (4.47)	1,832,830 (1.86)	8.13	5.42	38.81	4.60	11	2
6.0	6,480,656 (6.58)	4,688,889 (4.76)	1,791,767 (1.82)	7.84	5.42	33.58	4.60	11	2
7.0	6,762,176 (6.86)	4,918,937 (4.99)	1,843,239 (1.87)	6.74	5.41	21.79	4.60	13	3
				Till					
2.5	2,913,946 (2.96)	2,308,212 (2.34)	605,734 (0.61)	5.80	5.40	45.27	5.08	4	1
3.0	2,944,175 (2.99)	2,349,515 (2.38)	594,660 (0.60)	6.01	5.40	47.60	5.06	5	1
3.5	2,992,728 (3.04)	2,426,240 (2.46)	566,488 (0.57)	6.08	5.38	49.21	5.00	5	1
4.0	3,029,281 (3.07)	2,477,618 (2.51)	551,663 (0.56)	6.31	5.37	51.55	5.00	5	1
5.0	3,113,824 (3.16)	2,594,330 (2.63)	519,494 (0.53)	6.46	5.35	54.12	5.00	3	2
6.0	3,291,233 (3.34)	2,747,742 (2.79)	543,491 (0.55)	6.40	5.33	52.36	5.00	3	2
7.0	3,381,191 (3.43)	2,861,376 (2.90)	519,815 (0.53)	6.43	5.31	48.91	5.00	4	2

† Number of large biopores and cracks in the biopore morphological dataset, classified by the validation.
‡ Values in parentheses are relative pore volumes as a percentage of the total pore volume.

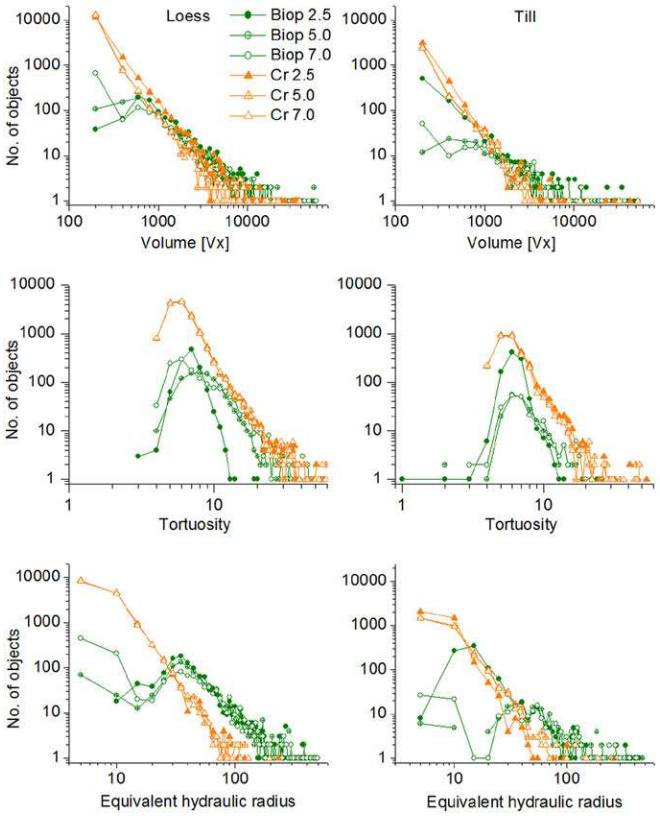

Fig. 9. Histograms of volume, tortuosity, and equivalent hydraulic radius for biopores (green) and cracks (orange) obtained from samples from the loess Bt and the till Bt samples for radii of the structuring element using in the speherical opening (E_D) = 2.5, 5.0, and 7.0. The radius of the structuring element used in the spherical opening (E_O) was kept constant at 2.5.

Corresponding object features (i.e., morphological pore properties) are presented in Table 7. Increasing E_D sizes resulted in a less clear separation of branches and loosely connected parts of the pore cluster (Fig. 10), underlined by increasing values of volume, surface, S/V, τ, and EHR (Table 4).

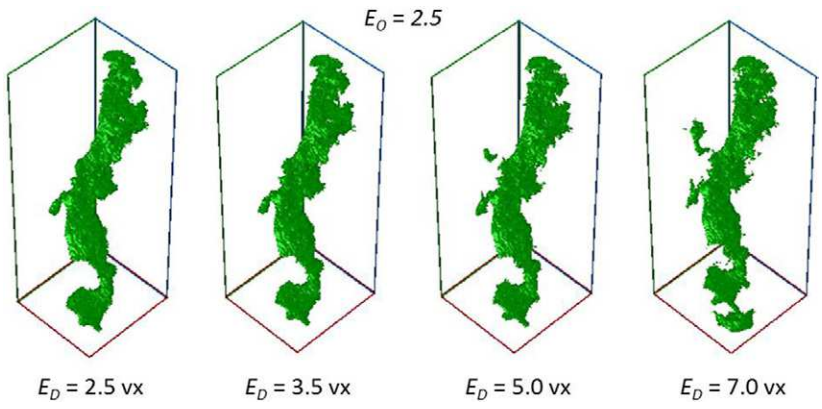

Fig. 10. Effects of increasing sizes of the radius of the structuring element used in the spherical dilation (E_D), visualized as an examplefor a single biopore (earthworm burrow segment) from the loess Bt sample. The radius of the structuring element used in the spherical opening (E_O) = 2.5 voxels (vx) in all cases. Frame size edge lengths: 70 by 70 by 201 vx (L by B by H; i.e., 16.2 by 16.2 by 46.4 mm).

Discussion

Workflow and Separation Method

The presented workflow (Fig. 1) yielded different 3D images and morphological datasets of biopores as well as of cracks and interaggregate spaces. In principle, the specific workflow steps could be conducted using alternative software (e.g., ImageJ, 3dma). However, the MAVI framework ToolIP offers a comfortable programming of different plugins enabling subsequent and parallel 3D image processing steps. As formal restrictions, ToolIP does not provide open access, the scientific community using it is small, and online tutorial help cannot be used yet.

As a remaining methodological problem, we consider the inclusion of thin biopores (i.e., worm burrows and root channels with small diameters) in the crack images (Fig. 6). Such an ambiguous assignment cannot be completely avoided. However, the validation of the separated morphological datasets by the straightforward algorithms using MS Excel (Tables 3 and 6, last columns) showed that the separation of the macropore types was correct for large pores in most cases. In terms of preferential flow, where large macropores are of highest relevance, possible misclassification of small pores will yield only small quantitative effects.

The general problem for each separation method based on shape parameters is to capture the complexity of real soil pores with relatively simple parameters. The interconnectedness between macropore types as clusters or networks contributes to this high morphological complexity. Although not perfect, the presented approach provides an alternative to the separation procedures based on frequency thresholds of, for example, the pore volume (Pagenkemper et al., 2013; Perret et al., 1999; Zhang et al., 2018). Its main advantages are the efficiency of image processing, which results in the simultaneously obtained images and morphological datasets and the preservation of the macropore surface roughness (Fig. 2). The parameters in the basic image processing steps of opening and dilation (sizes of E_O and E_D) can be alternated step by step. This enables the quantitative assessment of effects of these procedures on the object properties of the 3D images and thus on the calculated morphological macropore properties, such as the pore volume. The method should be complemented by visual inspection of the 3D images. However, in turn it can also be used to "calibrate" visual inspection by relatively objective parameters.

Optimizing Procedure for E_O and E_D

The general decrease in V_{tot} and S_{tot} with increasing E_O sizes (Table 2) is caused by the increasing elimination of smaller objects (i.e., pores) by the spherical opening algorithm (i.e., it is determined by E_O). Greater E_O sizes resulted in smaller numbers of pores with greater median values for volumes and surface areas (Fig. 5). Although the smallest E_O sizes (1.5 and 2.0 vx) yielded the highest S_{tot} and V_{tot} (Tables 2 and 3), suggesting maximum separation efficiency, it was proven by the application of shape factors (Fig. 4)

Table 7. Volume, surface area, shape factors (f_1,f_2,f_3), surface/volume ratio (S/V), tortuosity (τ), and equivalent hydraulic radius (EHR) calculated for an individual biopore (earthworm burrow segment) from the loess sample after application of different sizes of the radius of the structuring element used in the spherical dilation (E_D) (E_O = 2.5 voxels in all cases). Data correspond to Fig. 10.

Size†		Volume	Surface area	f_1	f_2	f_3	S/V	τ	EHR
E_O	E_D	voxels	pixels						
2.5	2.5	49,103	19,318	0.194	0.005	0.085	0.393	9.07	263.99
2.5	3.5	50,707	21,148	0.175	0.002	0.054	0.417	11.82	271.16
2.5	5.0	53,242	24,083	0.151	0.001	0.031	0.452	16.62	284.72
2.5	7.0	59,676	29,793	0.123	0.000	0.019	0.499	22.15	296.90

† E_O, radius of the structuring element used in the spherical opening.

and by visual inspection (Fig. 6 and 7) that these E_O sizes did not result in a sufficient separation between biopores and cracks. As a consequence of the greater biopores that were caused ("opened") by greater E_O sizes, the median values of the EHR strongly increased, whereas the effects on τ were small (Table 3). This appears plausible because EHR depends on the pore volume (Eq. [6]), which is strongly affected by E_O, whereas τ is determined by the pore lengths (Eq. [5]), which are less affected by E_O.

The increase of V_{tot} and S_{tot} with increasing E_D sizes is caused by the fact that greater E_D sizes preserved more biopores as well as cracks in the surrounding of the biopores (Fig. 10) after the masking of the Fill-Hole image (Fig. 2b) by the dilation image (Fig. 2d). This effect was more pronounced for biopores than for cracks (Fig. 9), which were more often either eliminated by the opening or connected to the biopores and thus identified as biopores.

The absolute or relative sizes of V, S, τ, and EHR were not useful for determining optimum sizes for E_O and E_D because their trends were continuous in most cases. In contrast, the criterion of maximized differences in the pore shape, expressed by $\delta S/V$ vs. δf_2 (Fig. 4 and 8), pointed at the optimum sizes of 2.5 vx for E_O and E_D. This was found plausible by visual inspection of the 3D images (Fig. 6, 7, and 10). At $E_O = E_D = 2.5$, the significantly different levels of S/V between biopores (0.7–0.8) and cracks (~1.8) highlight the suitability of this shape parameter for a differentiation of macropore types. The equal size of the two parameters E_O and E_D appeared reasonable in the shown approach because both processing steps are complemental to each other.

Applicability to Other Spatial Resolutions

Although the optimum sizes of E_O and E_D were the same for the 3D images of the two shown soils, they may differ for other soils with respect to the size, texture, and structure of the soil sample as well as to the scientific question. However, the proposed principle is based on voxels and thus is expected to be applicable to 3D image data of different spatial resolutions (i.e., of different voxel edge lengths as determined by sample size and XRCT measurement settings).

The relatively coarse spatial resolution of 231-μm voxel edge length used here is an artificial threshold determined by the soil core diameter and the XRCT technique. Smaller sample sizes will enable a higher voxel resolution (i.e., smaller voxel edge lengths). However, such small pores are probably disconnected to preferential flow paths. We expect the spatial resolution of 231 μm to be sufficient with respect to preferential flow, even when removing pores up to volumes of 0.246 mm^3 (i.e., 20 vx). For (mean) pore diameters of 231 μm, the corresponding pressure head would be approximately −12.7 cm. In previous studies of loess-derived Luvisol, macrocapillary pore diameters between 1470 and 40 μm were found that corresponded to pressure heads between −2 and −70 cm (e.g., Kodešová et al., 2012). In most studies, rapid nonequilibrium flow is reported predominantly for pores larger than ~300 μm (Jarvis et al., 2007; Perret et al., 1999), corresponding to pressure heads of −10 cm and lower. However, another previous study at Hnevceves, Czech Republic (Kodešová et al., 2011), showed that preferential transport also took place between aggregates (i.e., in pores <231 μm). Thus, the XRCT measurement resolution of 231 μm vx edge length is coarser than the diameter of small pores in which preferential flow likely can take place. However, this measurement resolution is able to show the major pathways (i.e., large macropores) that have the greatest preferential transport capacity and thus are most relevant. We assume the size of the sampled soil cores and the size of the macropore to be at the level of the representative elementary volume. However, further studies using the proposed method should test different core sizes (i.e., data set sizes) for determining optimized sample sizes with respect to the representative elementary volume.

Conclusion

We present a voxel-based method for separating biopores from cracks and interaggregate spaces in 3D image data obtained from XRCT measurements of soil cores. As crucial steps in the image processing workflow, the structuring element sizes in both the spherical opening and dilation procedure could be determined more objectively and independently based on structural parameters. Maximum differences between biopores and cracks considering two shape factors (i.e., S/V and f_2) related to the size of the structuring element appeared useful for the determination of such parameter values. Differences in the trends of V, S, τ, and EHR between the sites and macropore types suggest site-specific and macropore type–specific sensitivities to the used 3D image processing steps. The separation procedure comprising structured

masking steps after spherical opening and dilatation allowed preserving the original macropore surface roughness in the 3D images. In addition to the potential for an objective determination of important parameters of 3D image processing, the approach enables to calculate and thus to assess quantitative effects of the parameter settings on relevant soil morphological parameters. The approach is applicable to different soils and adjustable to 3D image data of different spatial resolution and is an alternative to other separation methods based on thresholds found in parameter frequency distributions. It appeared useful as preprocessing step for a subsequent quantification of physicochemical surface properties of different macropore types for soil volumes, enabling a more precise description of preferential flow and transport.

Acknowledgments

This study was funded by the Deutsche Forschungsgemeinschaft (DFG), Bonn, Germany, under grant LE 3177/1-2: "Quantification of small-scale physicochemical and microbiological properties of intact macropore surfaces in structured soils."

References

Bundt, M., F. Widmer, M. Pesaro, J. Zeyer, and P. Blaser. 2001. Preferential flow paths: Biological 'hot spots' in soils. Soil Biol. Biochem. 33:729–738. doi:10.1016/S0038-0717(00)00218-2

Capowiez, Y., S. Sammartino, and E. Michel. 2011. Using X-ray tomography to quantify earthworm bioturbation non-destructively in repacked soil cores. Geoderma 162:124–131. doi:10.1016/j.geoderma.2011.01.011

Don, A., B. Steinberg, I. Schöning, K. Pritsch, M. Joschko, G. Gleixner, and E.-D. Schulze. 2008. Organic carbon sequestration in earthworm burrows. Soil Biol. Biochem. 40:1803–1812. doi:10.1016/j.soilbio.2008.03.003

Feldkamp, L.A., L.C. Davis, and J.W. Kress. 1984. Practical cone-beam algorithm. J. Opt. Soc. Am. A 1:612–619. doi:10.1364/JOSAA.1.000612

Fér, M., and R. Kodešová. 2012. Estimating hydraulic conductivities of the soil aggregates and their clay-organic coatings using numerical inversion of capillary rise data. J. Hydrol. 468–469:229–240. doi:10.1016/j.jhydrol.2012.08.037

Fér, M., R. Kodešová, O. Golovko, Z. Schmidtová, A. Klement, A. Nikodem, et al. 2018. Sorption of atenolol, sulfamethoxazole and carbamazepine onto soil aggregates from the illuvial horizon of the Haplic Luvisol on loess. Soil Water Res. 13:177–183. doi:10.17221/82/2018-SWR

Fraunhofer Institute for Industrial Mathematics. 2012. MAVI: Modular Algorithms for Volume Images V1.4.1. Fraunhofer Institute for Industrial Mathematics, Kaiserslautern, Germany.

Gerke, H.H. 2012. Macroscopic representation of the interface between flow domains in structured soil. Vadose Zone J. 11(3). doi:10.2136/vzj2011.0125

Iassonov, P., T. Gegrenegus, and M. Tuller. 2009. Segmentation of X-ray computed tomography images of porous materials: A crucial step for characterization and quantitative analysis of pore structures. Water Resour. Res. 45:W09415. doi:10.1029/2009WR008087

Jarvis, N. 2007. A review of non-equilibrium water flow and solute transport in soil macropores: Principles, controlling factors and consequences for water quality. Eur. J. Soil Sci. 58:523–546. doi:10.1111/j.1365-2389.2007.00915.x

Jarvis, N., M. Larsbo, S. Roulier, A. Lindahl, and L. Persson. 2007. The role of soil properties in regulating non-equilibrium macropore flow and solute transport in agricultural topsoils. Eur. J. Soil Sci. 58:282–292. doi:10.1111/j.1365-2389.2006.00837.x

Kodešová, R., V. Jirků, V. Kodeš, M. Mühlhanselová, A. Nikodem, and A. Žigová. 2011. Soil structure and soil hydraulic properties of Haplic Luvisol used as arable land and grassland. Soil Tillage Res. 111:154–161. doi:10.1016/j.still.2010.09.007

Kodešová, R., K. Němeček, V. Kodeš, and A. Žigová. 2012. Using dye tracer for visualization of preferential flow at macro- and microscales. Vadose Zone J. 11(1). doi:10.2136/vzj2011.0088

Kuzyakov, Y., and E. Blagodatskaya. 2015. Microbial hotspots and hot moments in soil: Concept & review. Soil Biol. Biochem. 83:184–199. doi:10.1016/j.soilbio.2015.01.025

Leue, M., K.-U. Eckhardt, R.H. Ellerbrock, H.H. Gerke, and P. Leinweber. 2016. Analyzing organic matter composition at intact biopore and crack surfaces by combining DRIFT spectroscopy and pyrolysis-field ionization mass spectrometry. J. Plant Nutr. Soil Sci. 179:5–17. doi:10.1002/jpln.201400620

Leue, M., K.-U. Eckhardt, H.H. Gerke, R.H. Ellerbrock, and P. Leinweber. 2017. Spatial distribution of organic matter compounds at intact macropore surfaces predicted by DRIFT spectroscopy. Vadose Zone J. 16(9). doi:10.2136/vzj2017.05.0111

Leue, M., and H.H. Gerke. 2016. Roughness of biopores and cracks in Bt-horizons assessed by confocal laser scanning microscopy. J. Plant Nutr. Soil Sci. 179:529–536. doi:10.1002/jpln.201600016

Leue, M., H.H. Gerke, and S.C. Godow. 2015. Droplet infiltration and organic matter composition of intact crack and biopore surfaces from clay-illuvial horizons. J. Plant Nutr. Soil Sci. 178:250–260. doi:10.1002/jpln.201400209

Leue, M., A. Wohld, and H.H. Gerke. 2018. Two-dimensional distribution of soil organic carbon at intact macropore surfaces in Bt-horizons. Soil Tillage Res. 176:1–9. doi:10.1016/j.still.2017.10.002

Lin, H. 2010. Linking principles of soil formation and flow regimes. J. Hydrol. 393:3–19. doi:10.1016/j.jhydrol.2010.02.013

Luo, L., H. Lin, and S. Li. 2010. Quantification of 3-D soil macropore networks in different soil types and land uses using computed tomography. J. Hydrol. 393:53–64. doi:10.1016/j.jhydrol.2010.03.031

Otsu, N. 1979. A threshold selection method from gray-level histograms. IEEE Trans. Syst. Man Cybern. 9:62–66. doi:10.1109/TSMC.1979.4310076

Pagenkemper, S.K., M. Athmann, D. Uteau-Puschmann, T. Kautz, S. Peth, and R. Horn. 2015. The effect of earthworm activity on soil bioporosity: Investigated with X-ray computed tomography and endoscopy. Soil Tillage Res. 146:79–88. doi:10.1016/j.still.2014.05.007

Pagenkemper, S.K., S. Peth, D. Uteau-Puschmann, and R. Horn. 2013. Effects of root-induced biopores on pore space architecture investigated with industrial X-ray computed tomography. In: S.H. Anderson and J.W. Hopmans, editors, Soil–water–root processes: Advances in tomography and imaging. SSSA Spec. Publ. 61. SSSA, Madison, WI. p. 69–96. doi:10.2136/sssaspecpub61.c4

Perret, J., S.O. Prasher, A. Kantzas, and C. Langford. 1999. Three-dimensional quantification of macropore networks in undisturbed soil cores. Soil Sci. Soc. Am. J. 63:1530–1543. doi:10.2136/sssaj1999.6361530x

Pierret, A., Y. Capowiez, L. Belzunces, and C.J. Moran. 2002. 3D reconstruction and quantification of macropores using X-ray computed tomography and image analysis. Geoderma 106:247–271. doi:10.1016/S0016-7061(01)00127-6

Rieckh, H., H.H. Gerke, J. Siemens, and M. Sommer. 2014. Water and dissolved carbon fluxes in an eroding soil landscape depending on terrain position. Vadose Zone J. 13(7). doi:10.2136/vzj2013.10.0173

Rieckh, H., H.H. Gerke, and M. Sommer. 2012. Hydraulic properties of characteristic horizons depending on relief position and structure in a hummocky glacial soil landscape. Soil Tillage Res. 125:123–131. doi:10.1016/j.still.2012.07.004

Rogasik, H., H. Weinkauf, and M. Seyfarth. 1997. Methodology and technology of sampling undisturbed soil cores. (In German with English abstract.) Arch. Acker-Pflanzenbau Bodenkd. 41:199–207.

Sammartino, S., A.-S. Lissy, C. Bogner, R. Van Den Bogaert, Y. Capowiez, S. Ruy, and S. Cornu. 2015. Identifying the functional macropore network related to preferential flow in structured soils. Vadose Zone J. 14(10). doi:10.2136/vzj2015.05.0070

Vecchio, I., K. Schladitz, M. Godehardt, and M.J. Heneka. 2012. 3D Geometric characterization of particles applied to technical cleanliness. Image Anal. Stereol. 31:163–174. doi:10.5566/ias.v31.p163-174

Vogel, H.J., U. Weller, and S. Schlüter. 2010. Quantification of soil structure based on Minkowski functions. Comput. Geosci. 36:1236–1245. doi:10.1016/j.cageo.2010.03.007

Wang, W., A.N. Kravchenko, A.J.M. Smucker, and M.L. Rivers. 2011. Comparison of image segmentation methods in simulated 2D and 3D microtomographic images of soil aggregates. Geoderma 162:231–241. doi:10.1016/j.geoderma.2011.01.006

Zhang, Z., K. Liu, H. Zhou, H. Lin, D. Li, and X. Peng. 2018. Three dimensional characteristics of biopores and non-biopores in the subsoil respond differently to land use and fertilization. Plant Soil 428:453–467 [erratum: 430(1–2):441]. doi:10.1007/s11104-018-3689-3

Zhang, Z.B., X. Peng, H. Zhou, H. Lin, and H. Sun. 2015. Characterizing preferential flow in cracked paddy soils using computed tomography and breakthrough curve. Soil Tillage Res. 146:53–65. doi:10.1016/j.still.2014.05.016